Electronic Supplementary Material (ESI) for Journal of Materials Chemistry B.
This journal is © The Royal Society of Chemistry 2017

Supporting Information

Via precise interface engineering toward bioinspired composites with improved 3D printing processability and mechanical properties

Felix Hanßke, Onur Bas, Cédryck Vaquette, Gernot Hochleitner, Jürgen Groll, Erhard Kemnitz, Dietmar W. Hutmacher, and Hans G. Börner**

* to whom correspondence is to be addressed

Prof. Dr. Hans Börner

Humboldt-Universität zu Berlin, Brook-Taylor-Str. 2, 12489 Berlin, Germany

E-Mail: h.boerner@hu-berlin.de

Phone: +49 (0)30-2093 7348

Fax: +49 (0)30 2093-7500

Content

Screening of sequence-specific compatibilizer peptides 3
Synthesis of peptide-PEG conjugates 3
Analysis of peptide-PEG conjugates 4
MBC: *H*-GGTQYYAYSTTQKS-*block*-PEG 4
MBC^{SC}: *H*-GGAKTSYTYQSTYQ-*block*-PEG 5
Synthesis of MgF_2 sol nanoparticles and composite preparation 6
3D Printing techniques 6
Fused deposition modeling (FDM) or melt extrusion 6
Melt electrospinning writing (MEW) 7
Scaffold characterization 7
Surface and bulk characterization 8
Crystallinity 8
Mechanical testing 10
Ion release 11
Accelerated degradation 12
In vitro compatibility 12
Cell culture 12
DNA quantification 12
Alkaline Phosphatase (ALP) activity 13
Statistical analysis 13
Supplementary figures 14

Screening of sequence-specific compatibilizer peptides

Peptides adhering on MgF_2 particles were screened from a phage display containing up to 10^9 different 12mer sequences. Screening and synthesis is described elsewhere in detail.[1] In short, a library of genetically modified bacteriophages (New England BioLabs, Ipswich, MA, USA) was incubated with 10 mg of MgF_2 particles. The particles were washed to elute weak binding phages from the inorganic surfaces. Stronger binding phages were eluted. These phages were amplified and incubated with particles again to repeat the biopanning cycle several times to enrich high-affinity adhesives.

Synthesis of peptide-PEG conjugates

The sequence with the best adhesion properties (*H*-GGTQYYAYSTTQKS-PEG_{73}) was synthesized as a peptide-PEG conjugate. Therefore, solid-phase supported peptide synthesis with ABI-Fastmoc protocols (ABI 433A synthesizer, Applied Biosystems, Life Technologies Corporation, Carlsbad, CA, USA) in *N*-methyl-2-pyrolidone (Iris Biotech, GER) was used on TentaGel® PAP resin ($M_{n,PEG}$ = 3200 g mol^{-1}, Rapp Polymere, GER). Conjugates were cleaved from solid support with TFA/Trimethylsilyl bromide = 99:1 (v/v) (Acros Organics, GER, and Iris Biotech, GER) for 6 h, purified by aqueous size-exclusion chromatography on HiTrap Desalting columns on an ÄKTAprime plus (both GE Healthcare Life Sciences, GER) and lyophilized. Analysis was performed by MALDI-ToF-MS (Matrix: α-Cyano-4-hydroxycinnamic acid (αCHCA), Sigma-Aldrich, GER, Bruker autoflex III smartbeam with matrix assisted laser desorption/ionization and time of flight detector, GER), ^1H NMR spectroscopy in TFA-d (Acros Organics) (Bruker AVANCE II 500, GER) and FT-ATR-IR spectroscopy with golden gate technique (Jasco FT/IR-4200, Easton, MD, USA).

Analysis of peptide-PEG conjugates

MBC: *H*-GGTQYYAYSTTQKS-*block*-PEG

(MgF_2-binding peptide-PEG conjugate)

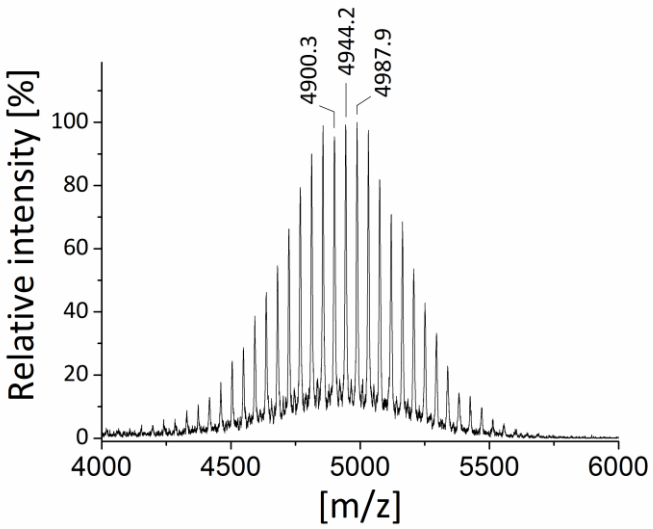

Figure S1. MALDI-ToF-MS of MBC.

MS (MALDI-ToF) *m*/*z*: $[M + H]^+$ calcd for $C_{222}H_{408}N_{18}O_{101}$, 4944.03; found, 4944.2;

Δm = 44 m/z, characteristic for repeating ethylene glycol (EG) units;

$M_{calcd} = M_{peptide} + M_{PEGn} + H$ = 4944.03 Da. The mass can be assigned within ± 0.2 m/z accuracy.

^{1}H NMR (500 MHz, TFA-*d*, δ): 7.30-6.83 (m, 12H; Ar H_Y), 5.40-4.25 (m, 28H; 2×$CH_{2,G}$, 6×CH_T, 2×CH_Q, 3×CH_Y, CH_A, 2×CH_S, 2×$CH_{2,S}$, CH_K), 4.15-3.81 (m, 304H; $CH_{2,PEG}$), 3.39-2.89 (m, 8H; 3×$CH_{2,Y}$, $CH_{2,K}$), 2.88-2.60 (m, 4H; 2×$CH_{2,Q}$), 2.60-2.17 (m, 4H; 2×$CH_{2,Q}$), 2.13-1.86 (m, 4H; 2×$CH_{2,K}$), 1.78-1.42 ppm (m, 14H; $CH_{2,K}$, 3×$CH_{3,T}$, $CH_{3,A}$);

ATR-IR: ν = 3276 (*m*; N-H Amid A), 2945-2860 (*vs*, C-H), 1623 (*s*, C=O Amid I), 1535 (*m*, N-H Amid II), 1466 (*m*, CH_2), 1359 (*m*, CH_2), 1096 cm^{-1} (s, C-O-C_{PEG}).

MBC^{SC}: *H*-GGAKTSYTYQSTYQ-*block*-PEG

(scrambled MgF_2-binding peptide-PEG conjugate)

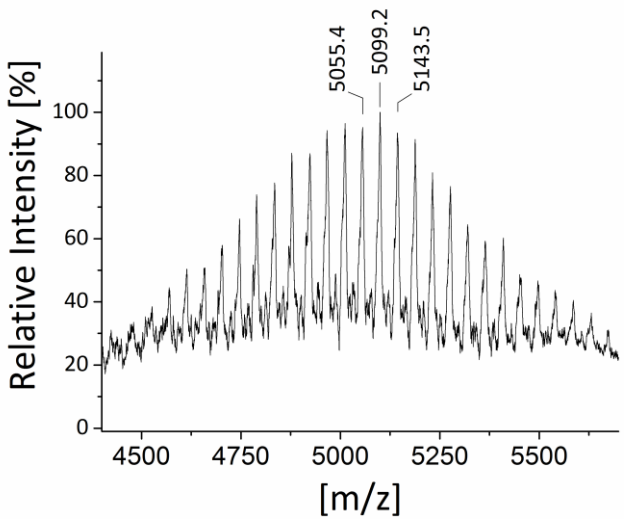

Figure S2. MALDI-ToF-MS of MBC^{SC}.

MS (MALDI-ToF) *m*/*z*: $[M + Na]^+$ calcd for $C_{226}H_{416}N_{18}O_{103}$, 5099.03; found, 5099.2;

Δm = 44 m/z, characteristic for repeating ethylene glycol (EG) units;

$M_{calcd} = M_{peptide} + M_{PEGn} + Na$ = 5099.03 Da. The mass can be assigned within ± 0.2 m/z accuracy.

^{1}H NMR (500 MHz, TFA-*d*, δ): 7.21-6.73 (m, 12H; Ar H_Y), 5.24-4.17 (m, 23H; 2×$CH_{2,G}$, 6×CH_T, 2×CH_Q, 3×CH_Y, CH_A, 2×CH_S, 2×$CH_{2,S}$, CH_K), 4.11-3.66 (m, 320H; $CH_{2,PEG}$), 3.32-3.21 (m, 2H; $CH_{2,K}$), 3.09-2.60 (m, 12H; 3×$CH_{2,Y}$, $CH_{2,K}$, 2×$CH_{2,Q}$), 2.37-1.81 (m, 10H; 2×$CH_{2,Q}$, 3×$CH_{2,K}$), 1.73-1.16 ppm (m, 12H; 3×$CH_{3,T}$, $CH_{3,A}$);

ATR-IR: ν = 3276 (*m*; N-H Amid A), 2945-2860 (*vs*, C-H), 1623 (*s*, C=O Amid I), 1535 (*m*, N-H Amid II), 1467 (*m*, CH_2), 1359 (*m*, CH_2), 1094 cm^{-1} (s, C-O-C_{PEG}).

Synthesis of MgF_2 sol nanoparticles and composite preparation

Applying standard Schlenk techniques Mg turnings (2.43 g, 100 mmol) were dissolved in 500 mL dried methanol (both Sigma-Aldrich) to yield $Mg(OCH_3)_2$ at a concentration of 0.2 M. A stoichiometric amount of methanolic HF (Solvay Fluor, GER) was added under continuous stirring. After aging for 2-3 weeks an optically clear sol of MgF_2 nanoparticles was achieved. ^{19}F NMR (300 MHz, locked in $CDCl_3$ in methanol, δ): -154 (BF_4^- from reaction of HF with glass vessel), -187 ($HF_{adsorped}$), -198 ppm (MgF_2). For composite mixing 3mol% of MBC (referred to n(MgF_2)) were incubated with MgF_2 sol for 4 h. PCL Capa 6500C (M_w = 50 kDa (manufacture's specification), Perstorp, SWE) was dissolved in tetrahydrofurane (50% (w/v)) at room temperature and compatibilized sol was added, vigorously stirred for 5 min and the solvent evaporated under reduced pressure. Dried composites were used for fabrication techniques.

3D Printing techniques

Fused deposition modeling (FDM) or melt extrusion

FDM scaffolds were processed by using a Bioextruder, a custom-made, melt extrusion based bioadditive manufacturing device, as described in detail elsewhere.[2] Briefly, sample materials were melted in a reservoir (120 °C), transported to a one-screw extruder by gas-pressure and printed at a temperature of 120 °C, deposition rate of ca. 25 µL min^{-1} through a 23G (0.34 mm inner diameter) nozzle and translational collector speed of 0.3 m min^{-1} in a layer-wise manner. 3D scaffolds with dimensions of 40 mm x 40 mm x 2.7 mm had a 0° - 90° lay-down pattern, filament spacing of 1.6 mm and slice thicknesses of 0.3 mm. Smaller 4 mm x 4 mm x 2.7 mm scaffolds were cut from larger ones and were used for further evaluations. Additionally, flat samples consisting of a layer of filaments printed side by side without pores (1 cm x 0.5 cm) were fabricated for contact angles (CAs) and surface zeta potential measurements. To exclusively examine the mechanical properties of different

materials without influence of architectural effects 2 cm long single filaments were printed for tensile tests using the same printing parameters applied for the scaffold fabrication.

Melt electrospinning writing (MEW)

The detailed device description was previously published.[3] The custom-made MEW device with a high voltage source (DX250R, EMCO, Hallein, Austria) and a controller (Digit Multimeter 2100, Keithley, Cleveland, USA) was used with a gas-pressured feeding system. Samples were processed at 120 °C, 10 to 12 kV acceleration voltage, 1.5 mm collector distance, 2.0 bar feeding pressure through a 23G spinneret and collected on a grounded translational aluminium stage. Chosen instrumental parameter combinations were set in accordance with stable fiber printing of pure PCL, particularly in order to avoid the processing instabilities pulsing and long beading.[4] The deposition of proof of concept scaffold (10 x 10 cm^2) was guided by G-code (MACH 3 CNS software, ARTSOFT, Livermore Falls, USA) with a designed x,y pore size of 1 x 1 mm^2.

Scaffold characterization

Scanning electron microscopy (SEM) was performed on gold-coated (150 s, 30 mA) scaffolds on a FEI Quanta 200 Environmental SEM operating at 10 kV to show morphologies. Overview photographs were taken with an Olympus digital camera. Particle distribution and porosity were examined by Xradia Micro XCT-400 system (Carl Zeiss, CA, USA), at 0.6 µm voxel size resolution for high resolution sections and 10 µm voxel size for macro scans and porosity determination. The X-ray source voltage and current were set to 40 kV and 250 µA, respectively. Exposure times per radiograph were in the range of 10 s for the high resolution scans, and 4 s for the macro scans. Approximately 1200 projections were collected for each scan as the sample rotated over 180°. The volume was reconstructed with the instrument software and was then exported to CTAn (SkyScan) for further 3D image analysis.

Surface and bulk characterization

Static (sessile drop method, n = 3) and dynamic (add and remove volume method, n = 3) contact angles were measured using a FTA200 Contact Angle and Surface Tension Instrument (Poly-Instruments Pty. Ltd., Australia) releasing and retracting degassed deionized water at 2 µL s^{-1}. Static, advancing and receding angles were extracted from photographs captured by a Sanyo digital camera with Fta32 Video 2.0 software (First Ten Angstrom Inc.). X-ray photoelectron spectroscopy (XPS) analysis was performed on FDM samples by using a non-monochromatic Mg Kα X-ray source (1253.6 eV, DAR 400, Omicron Nanotechnology) in ultra-high vacuum below $1 * 10^{-10}$ mbar with a 125 mm hemispherical electron energy analyzer (Sphera II, 7 channels, Omicron Nanotechnology). Survey scans were taken at analyzer pass energy of 50 eV and high resolution scans at 20 eV. Gaussian/Lorentzian peak fitting with 20% Gauss character was used. Surface zeta potential was measured on Zetasizer Nano ZSP in an aqueous tracer solution (Malvern Instruments, UK). Elemental composition was studied by CHN analysis at HU Berlin on a Leco CHNS-923 analyzer.

Crystallinity

In search for a better understanding of the mechanical reinforcement crystallinities of the composites were investigated. These were analyzed by means of dynamic scanning calorimetry (DSC), X-ray diffraction (XRD) and Raman spectroscopy. Degrees of crystallinity X_C were calculated from the first two techniques (Figure S6). Integrated heating curves resulted in X_C (DSC) values between 59% (PCL) and 42% (PCL/MBC). 1wt% $cMgF_2$ was comparable to PCL within error margins (58%), while X_C of higher compatibilized filling ratios decreased. Non-treated MgF_2 lowered X_C slightly (55%) in comparison to pure PCL. XRD of scaffolds was measured in transmission and the ratio of sharp, crystalline reflexes (at 21.3 and 23.7° 2θ) and the amorphous halo yielded X_C (XRD). Here, a similar trend as in DSC became obvious. X_C (XRD) of PCL (56%), 1wt% $cMgF_2$ (57%) and 1wt% $pMgF_2$ (57%) were

comparable and percentages for composites with increasing particle ratios decreased slightly from 53% to 50%. Interestingly, X_C (XRD) of PCL/MBC did not decrease significantly. These changes in crystallinity could be observed qualitatively via Raman spectroscopy as well (Figure S9). Distinct Raman bands assigned to crystalline or amorphous vibrations, respectively, allowed conclusions about the composites' crystallinities. Most useful for crystallinity characterization was the isolated band between 1710 and 1750 cm^{-1} caused by C=O stretching vibrations of the ester bonds.[5] The more intense band at 1724 cm^{-1} was assigned to crystalline PCL areas while amorphous PCL exhibited shifted responses at 1738 cm^{-1}. More differences on the molecular level could be seen from the broad bands around 865 cm^{-1}.[6] This broadening is indicative for more amorphous materials. For the compatibilized composites trends for increasingly amorphous PCL parts with higher filler ratios were concluded from broadened 1724 cm^{-1} bands, increased intensities and band shifts around 865 cm^{-1} (Figure S9). Crystallite sizes derived from X-ray diffractograms using Scherrer's equation ranged between 27 nm and 29 nm.[7]

DSC analysis was performed in 40 µL alumina pans using a Mettler Toledo 821e at heating/cooling rates of 10 °C min^{-1}. 3 heating/cooling cycles were performed between -65 to 120 °C. Samples were allowed to reach thermal equilibrium for 5 min between the runs. X_C was derived from the first heating cycle to include the thermal history after FDM printing. X_C was calculated according to the following equation (1).

$$X_C = \Delta H_f * \%_{PCL}^{-1} * \Delta H°_f^{-1} \quad (1)$$

where ΔH_f and $\Delta H°_f$ are the measured heat of fusion of the samples (normed to PCL content $\%_{PCL}$) and the heat of fusion of 100% crystalline PCL (136 J g^{-1}), respectively.[5, 8] XRD measurements were performed on scaffold cuts in transmission geometry on a STOE MP diffractometer (STOE & Cie, GER) between 5 - 65° 2θ (stepsize 0.6, 120 s/step) without background subtraction. To calculate X_C from the integral ratio of sharp, crystalline reflexes at 21.3 and 23.7° 2θ (attributed to the [110] and [200] planes)[9] I_{cryst} and amorphous halo I_{amorph}

the diffractograms were integrated by DIFFRAC.EVA software (Bruker) following the equation (2).

$$X_C = I_{cryst} * (I_{cryst} + I_{amorph})^{-1} \quad (2)$$

Raman spectra (n = 5) were recorded on a Renishaw InVia Raman system excited by a 785 nm laser line between 600 – 1850 cm^{-1} with 10% laser power (30 mW), 40 s acquisition time and accumulation of 8 spectra per spot. Focus was adjusted by a 50x objective lens with a 1200 groove mm^{-1} grating and scattering was recorded with a Ren-Cam CCD detector. Scherrer's equation (3)

$$\text{Crystallite size} = K \lambda \Delta(2\theta)^{-1} \cos(\theta)^{-1} \quad (3)$$

with the full width at half maximum Δ at 2θ, a shape factor $K = 1$ and the X-ray wavelength λ helped to estimate the crystallite mean size of crystalline domains in the composites from XRD patterns.[7]

Mechanical testing

Tensile and compressive mechanical properties of the specimens were characterized using an Instron 5848 microtester equipped with 5 N or 500 N load cells (Instron, AUS), respectively. For tensile modulus $E_{tensile}$ and tensile toughness measurements single filaments (n = 8, initial length l_0 = 10 mm) were elongated to break or maximal to 110 mm at a displacement rate of 100 mm min^{-1}. Toughness values were calculated as the integral below the stress-strain curves and are based on this 110 mm elongation because of the instrument's limited stretch length and are therefore referred to tensile toughness $U_T^{1000\%}$. 4 mm x 4 mm x 2.7 mm scaffolds were axially compressed to 20% of individual height at a displacement rate of 1 mm min^{-1} to obtain the compressive moduli $E_{compression}$ of the scaffolds (n = 8). Both compressive and tensile moduli were determined from the linear region of the slope of the stress-strain curve between approx. 0 – 5% strain which yielded a coefficient of determination $R^2 > 0.99$. The dimensions of the scaffolds and the single filaments were determined by an environmental

SEM TM-3000 without surface coating (Hitachi, Tokyo, JPN) and a Nikon Eclipse Ti Fluorescence Microscope (Nikon, Tokyo, JPN), respectively, to normalize the measured forces. Microindentation measurements of dense samples (n = 6) were performed on a Hysitron TI 950 Triboindenter (cono-spherical 5 µm, 60° conical probe). The specimens were probed in a rectangular grid with spot distances of at least 200 µm. The same maximum indenter displacement of 1000 nm was applied to all samples. Indentation moduli E_{indent} and ion hardness H values were evaluated from the load-depth indentation curves using the Oliver and Pharr method.[10] H is a function of contact depth h_c and defined as maximum load-to-indentation area quotient (3).

$$H = P_{max}\, A(h_c)^{-1} \tag{3}$$

The reduced elastic moduli E_r from the Hysitron software were converted to E_{indent} according to equation (4).

$$E_r^{-1} = (1 - \nu_i^2)\, E_i^{-1} + (1 - \nu_s^2)\, E_{indent}^{-1} \quad (4),$$

where ν_s is the Poisson's ratio of the samples, E_i = 1140 GPa is the elastic modulus and ν_i = 0.07 is the Poisson's ratio of the indenter tip. ν_s, ratio of the radial to axial strain, of different samples were calculated via optical measurements on 20% compressed, solid discs (2 mm diameter x 1 mm height).

Ion release

Induced coupled plasma-optical emission spectroscopy (ICP-OES) was measured from the supernatants of scaffold cuts incubated in 10 mL minimum essential medium (MEM) without magnesium (Corning, NY, USA) in which 0.1 g L^{-1} calcium chloride (Sigma) was added after purchase. Mg, Ca and P content was determined on a Varian ICP-OES Spektrometer 725 with radial torch (Palo Alto, CA, USA). Energy dispersive X-ray spectroscopy (EDX) (TM-1000, Hitachi High-Technologies Europe, Krefeld, GER) was used to monitor surface modifications after incubation in MEM.

Accelerated degradation

The accelerated degradation was executed with the FDM scaffolds according to a method described by Lam et al. which enables studying PCL degradation on a reasonable time scale.[11] Scaffolds (n = 6) were immersed in 5 M aqueous sodium hydroxide solution at 37 °C. At designated time points, materials were rinsed with deionized water several times and dried under reduced pressure for 24 h. The decreasing mass of scaffolds was measured using an electronic balance (0.1 mg resolution). Optical appearance and SEM morphology of exemplary scaffolds were documented (Olympus camera and TM-3000, see above).

In vitro compatibility

Cell culture

Cell source: Human placental MSC were utilized for this study. Primary human MSCs were isolated via enzymatic digestion according to established literature protocols and the study was approved by the Human Research Ethics Committee (HREC/09/QRBH/14).[12] The cells were cultured in Minimum Essential Medium Eagle – alpha modified (α-MEM) enriched with 10% of fetal calf serum (FCS), 1% penicillin/streptomycin until passage 7.

Scaffold seeding: Human placental MSC (50,000 cells in 30 µL of media) were seeded onto the FDM scaffolds and allowed to adhere for 4 h at 37 °C in a 5% CO_2 atmosphere before the well was filled with media. The scaffolds were further cultured for 2, 4 and 10 weeks in osteogenic media (100 µg/mL ascorbate-2-phosphate, 10 mM β-glycerophosphate, 0.1 µM dexamethasone). Two groups were created, a control group made of PCL and a test group made of the 1wt% $cMgF_2$.

DNA quantification

DNA content (n = 6 for each group) was measured at 2, 4 and 10 weeks post seeding. For cellular DNA content analysis, the remaining media was removed from the wells and the

samples were frozen at -80 °C for at least 48 h. The scaffolds were then placed in 1.5 mL Eppendorf tubes containing 300 µL of Proteinase K (Invitrogen) (Proteinase K/phosphate buffered EDTA (PBE) 0.5 mg/ml), at 60°C for 12 hours. The solution was thereafter diluted at a ratio of 1/15 in Phosphate Buffered EDTA PBE, and 100 µL was aliquoted in triplicates into black 96-well plates, and 100 µL of PicoGreen (P11496, Invitrogen) working solution was added. After 5 min incubation in the dark, the fluorescence (excitation 485 nm, emission 520 nm) was measured using a fluorescence plate reader. A standard curve of known λ DNA concentrations ranging from 10 ng/ml to 1 µg/mL was used to calculate the final DNA content of the sample.

Alkaline Phosphatase (ALP) activity

ALP activity (n = 6 was each group) was measured from the media in triplicate at different time-points (2, 4 and 10 weeks) after a 24 h release period. Briefly, samples were first immersed for 5 min in Dulbecco's Modified Eagle Medium (DMEM) without phenol red and this was repeated three times. They were then transferred to a new 24-well plate and 600 µL of this media was added before the samples were placed back in the incubator for precisely 24 h. ALP activity was measured using the SigmaFAST™ kit, as per the manufacturer's instructions. 100 µL of *p*-Nitrophenyl phosphate in Tris-base buffer was added to 100 µL of the culture media in a 96-well plate, and incubated at 37 °C and 5% CO_2 for another 24 h. At the end of the second incubation period, the plate was brought back to ambient temperature (20 °C) for 5 min and the absorbance was read at 405 nm using a plate reader (Benchmark Plus™ microplate spectrophotometer, BIO RAD). The ALP absorbance was normalized by the DNA content of each sample.

Statistical analysis

All values represent mean values ± standard deviations. Sample numbers are stated in the sections of the respective techniques. One-way ANOVA (OriginPro 9.1) was used to make pairwise comparisons between the means of composition groups.

Supplementary figures

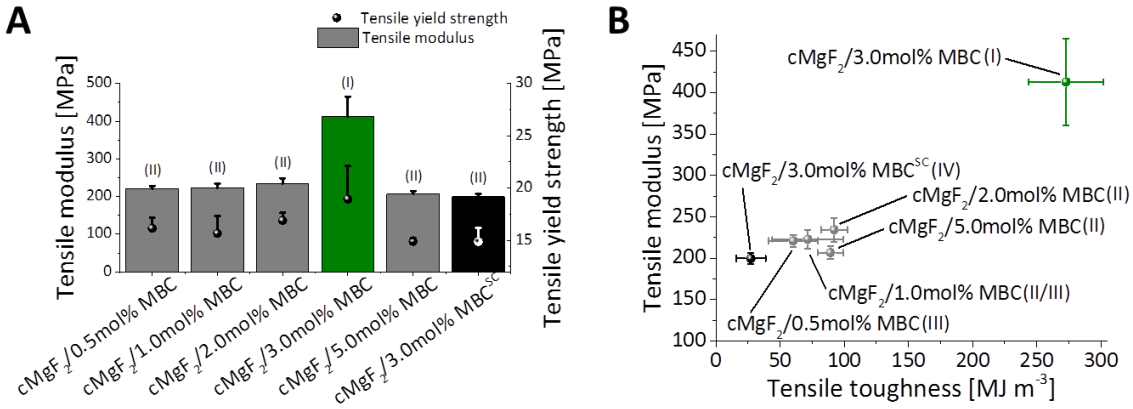

Figure S3. Mechanical reinforcement of compatibilized composite materials, variation of compatibilizer amounts in mol% referred to MgF_2 content: (A) Tensile moduli and yield strengths from tensile tests, (B) Tensile modulus-toughness diagram to underline simultaneous increase of stiffness and toughness in compatibilized samples. Low performance of scrambled reference conjugate MBC^{SC} highlights the importance of the peptide sequence for a successful material reinforcement by internal interface engineering (tensile toughness until maximum of 1000% elongation; Roman numerals (I) - (IV) classify the elastic moduli of (A) and the tensile toughnesses of (B) into groups that are significantly different by $p > 0.05$).

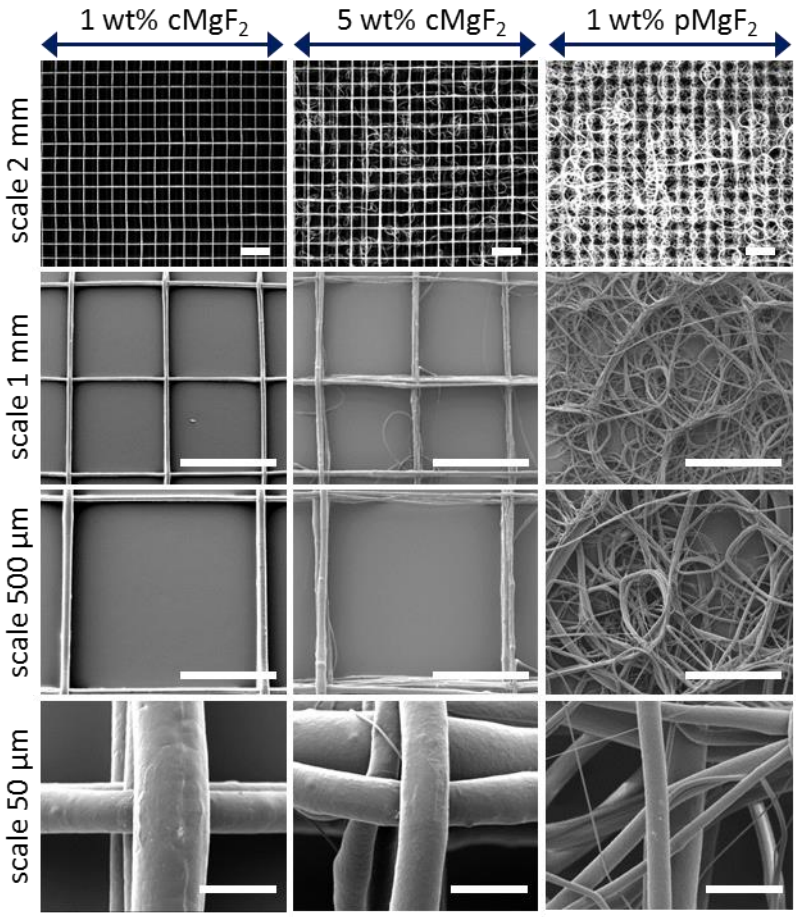

Figure S4. SEM overview of MEW printed scaffolds: Defined deposition/direct writing mode was possible with compatibilized composites (left and middle column) while non-compatibilized samples had nearly random deposition (right column).

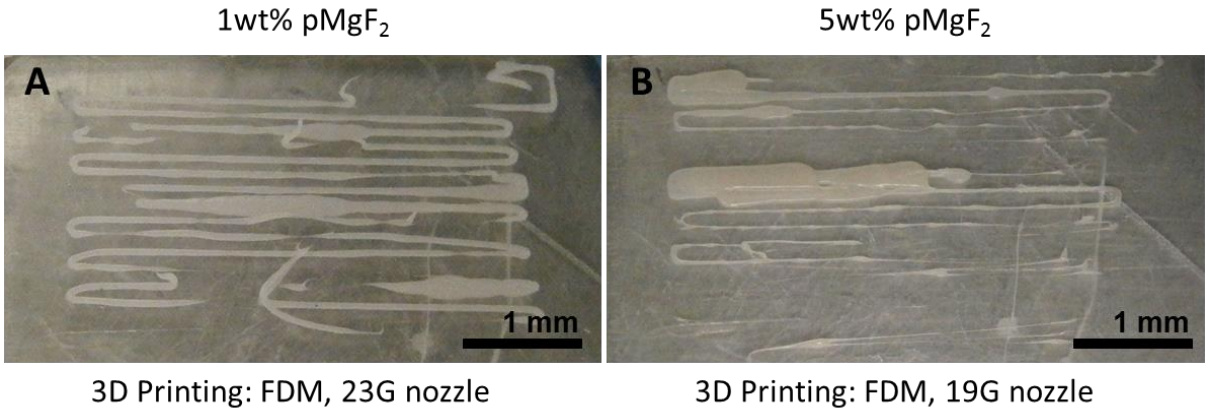

Figure S5. Photographs of failed FDM trials due to discontinuous printing: (A) Clogging occurred for 1 wt% $pMgF_2$ prior before printing the scaffolds, which may be an explanation for the reduction of $pMgF_2$ fraction in the printing process (cf. Figure 2 & Table S1). (B) For amounts ≥ 5 wt% $pMgF_2$ clogging happened more often and more severe even after changing to larger gauge sizes (up to 19G, 0.69 mm inner diameter).

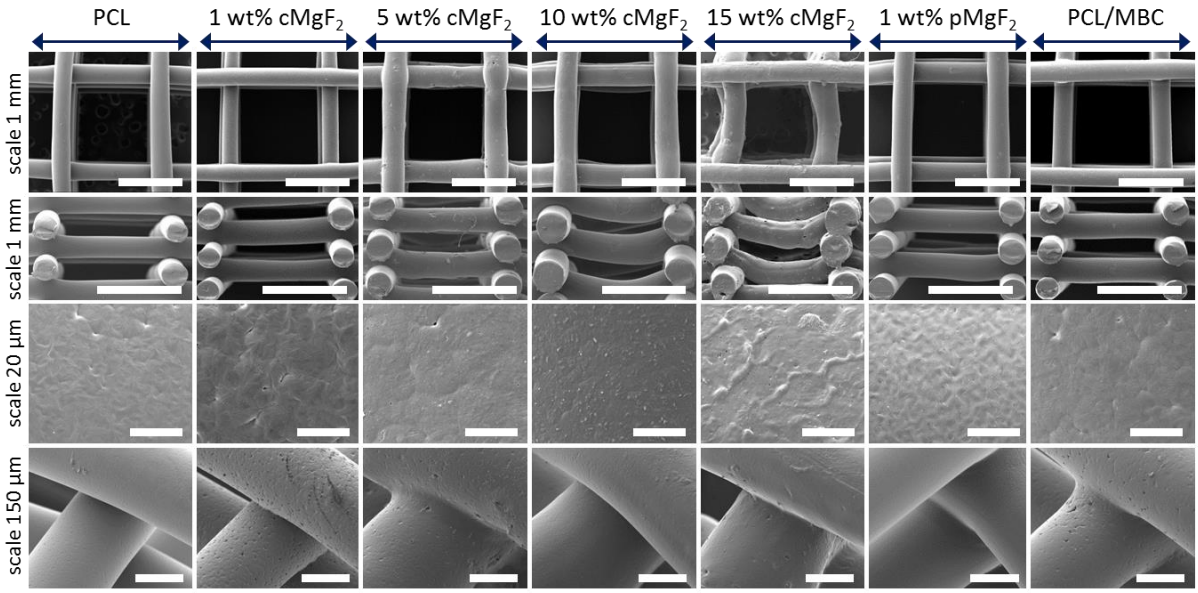

Figure S6. SEM overview of all FDM scaffolds: top view (first row), side view (second row), on top morphology (third row), interconnection of filaments (fourth row). All compositions could be 3D printed to the intended architecture, but filaments in composites with filler fractions of ≥ 10 wt% $pMgF_2$ showed sagging because of the difference in melt viscosities and the constant printing parameters. This highlights the importance of both tensile and compression tests to evaluate the mechanical materials properties. Uniaxial compression tests on the scaffolds are closer to applications in bone tissue engineering, while tensile tests of single filaments are more suited to probe the reinforcement of the composite material without network effects, e. g. caused by sagging.

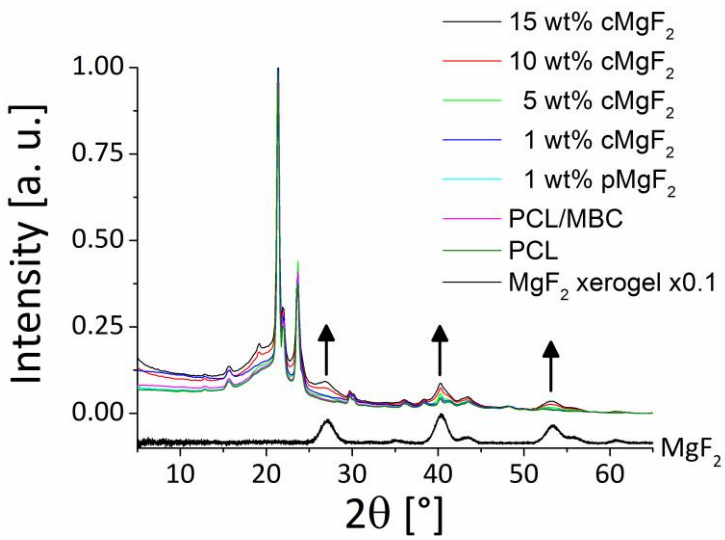

Figure S7. X-ray diffractograms of $pMgF_2$ xerogel (lower black line), PCL and PCL composite materials: Broad reflexes at 27.1°, 40.4° and 53.4° increased due to the presence of higher filling ratios of MgF_2 particles (arrows).

Table S1. Elemental composition measured by CHN analysis of PCL, 1 wt% $cMgF_2$ and 1 wt% $pMgF_2$.

Sample	theoretical[a)]			
	C [%]	H [%]	O [%]	**MgF_2 [%]**
PCL	63.2	8.8	28.0	**0.0**
PCL/1wt% $cMgF_2$	62.5	8.7	27.8	**1.0**
PCL/1wt% $pMgF_2$	62.8	8.7	27.8	**1.0**

Sample	measured before FDM printing				measured after FDM printing			
	C [%]	H [%]	O [%][b)]	**MgF_2 [%][c)]**	C [%]	H [%]	O [%][b)]	**MgF_2 [%][c)]**
PCL	-	-	-	**-**	63.2±0.1	8.8±0.1	28.1±0.1	**-**
PCL/1wt% $cMgF_2$	62.7±0.1	8.8±0.1	27.8±0.1	**0.7 ± 0.1**	62.4±0.1	8.8±0.1	27.8±0.1	**1.0±0.1**
PCL/1wt% $pMgF_2$	62.6±0.1	8.8±0.1	27.8±0.1	**1.0 ± 0.1**	62.9±0.1	8.8±0.1	27.9±0.1	**0.4±0.1**

[a)] theoretical PCL composition $(C_6H_{10}O_2)_n$ and intended $w(MgF_2)$; [b)] calculated from the molecular composition of PCL $(C_6H_{10}O_2)_n$ based on measured w(carbon); [c)] calculated from the molecular composition of PCL $(C_6H_{10}O_2)_n$ based on the mass difference between weight portion and found w(carbon); mean ± SD.

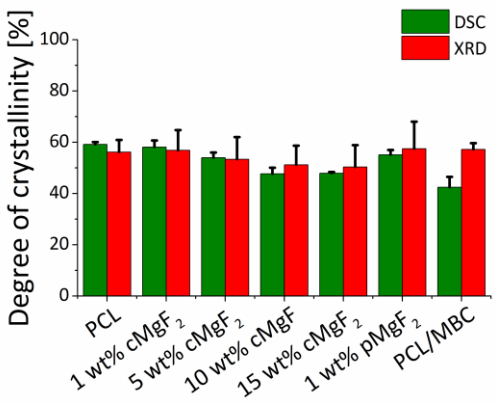

Figure S8. Degrees of crystallinity X_C calculated from DSC and XRD: Only small changes in the degrees of crystallinity X_C were observed in the composites, which are too less to be the main reason for the mechanical reinforcements.

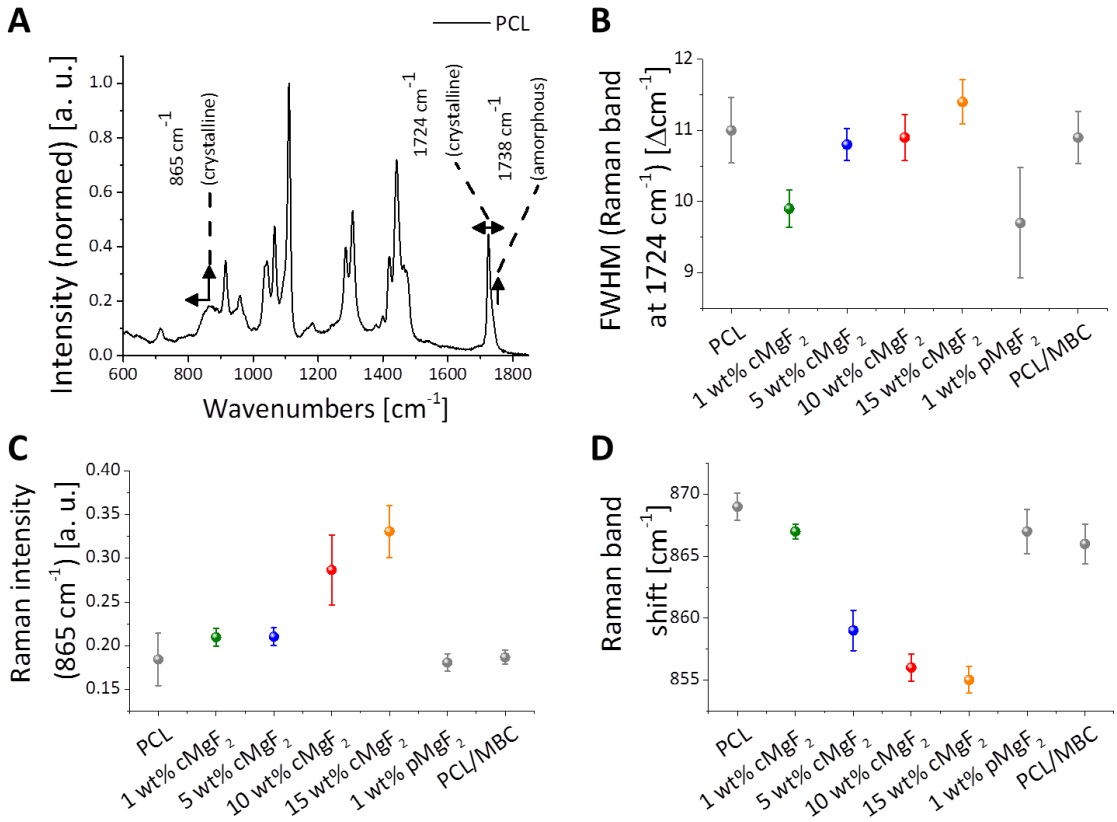

Figure S9. Crystallinity induced changes measured by Raman spectroscopy: (A) Typical spectrum of pure PCL with indicated changes that occur in PCL/MgF_2 composite materials. (B) Full width at half maximum (FWHM) of band at 1724 cm^{-1} influenced by a more prominent band assigned to amorphous PCL at 1738 cm^{-1}. (C) Raman intensity at 865 cm^{-1} assigned to amorphous PCL. (D) Shift of Raman band around 865 cm^{-1} assigned to amorphous PCL.

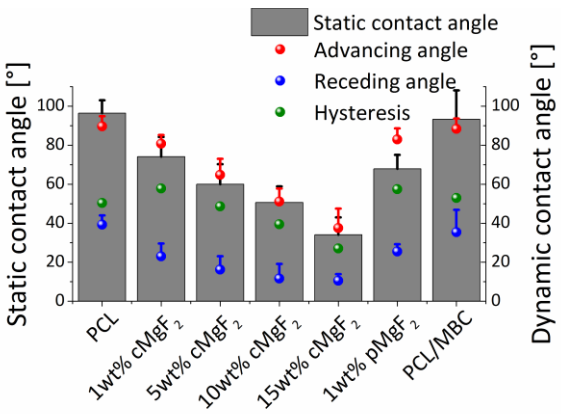

Figure S10. Contact angles of melt extruded PCL and composite materials: Measurements in both static and dynamic mode showed the same trend. Samples without MgF_2 were highly hydrophobic which is typical for PCL, while the contact angles decreased with increasing content of MgF_2. Hysteresis is the difference between advancing and receding angles from the dynamic measurements.

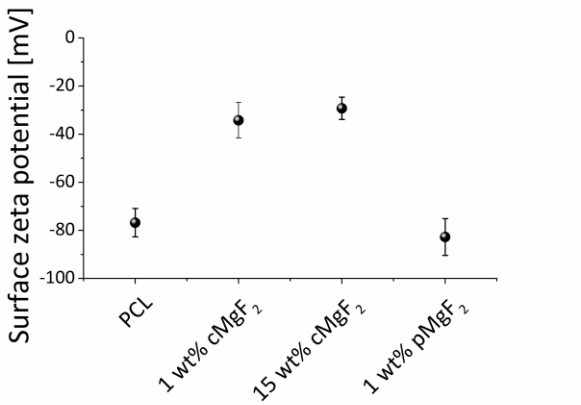

Figure S11. Surface zeta (ζ)-potential of FDM scaffolds in aqueous tracer solution: Only $cMgF_2$ (almost independent of the filler fraction) was able to neutralize the surface ζ-potential of the composites, which might reduce repulsive effects at the composites surfaces.

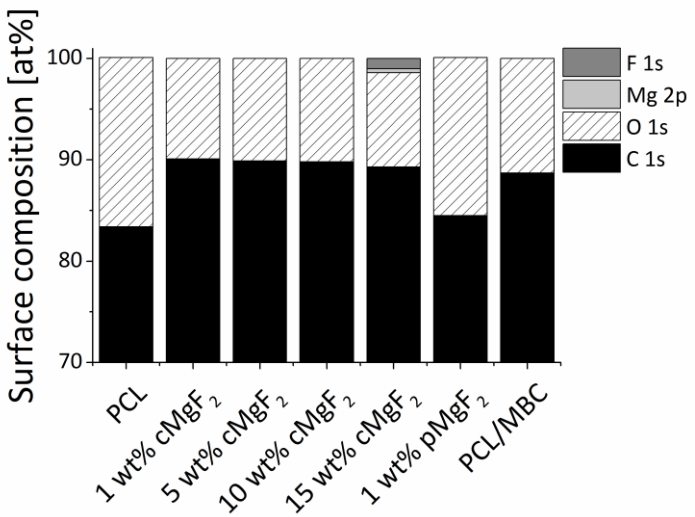

Figure S12. Elemental surface composition derived from XPS survey scans: Only 15 wt% $cMgF_2$ showed integrable Mg 2p and F 1s binding energies. According to these measurements, MgF_2 particles were completely embedded in the PCL matrix (except for 15 wt% $cMgF_2$).

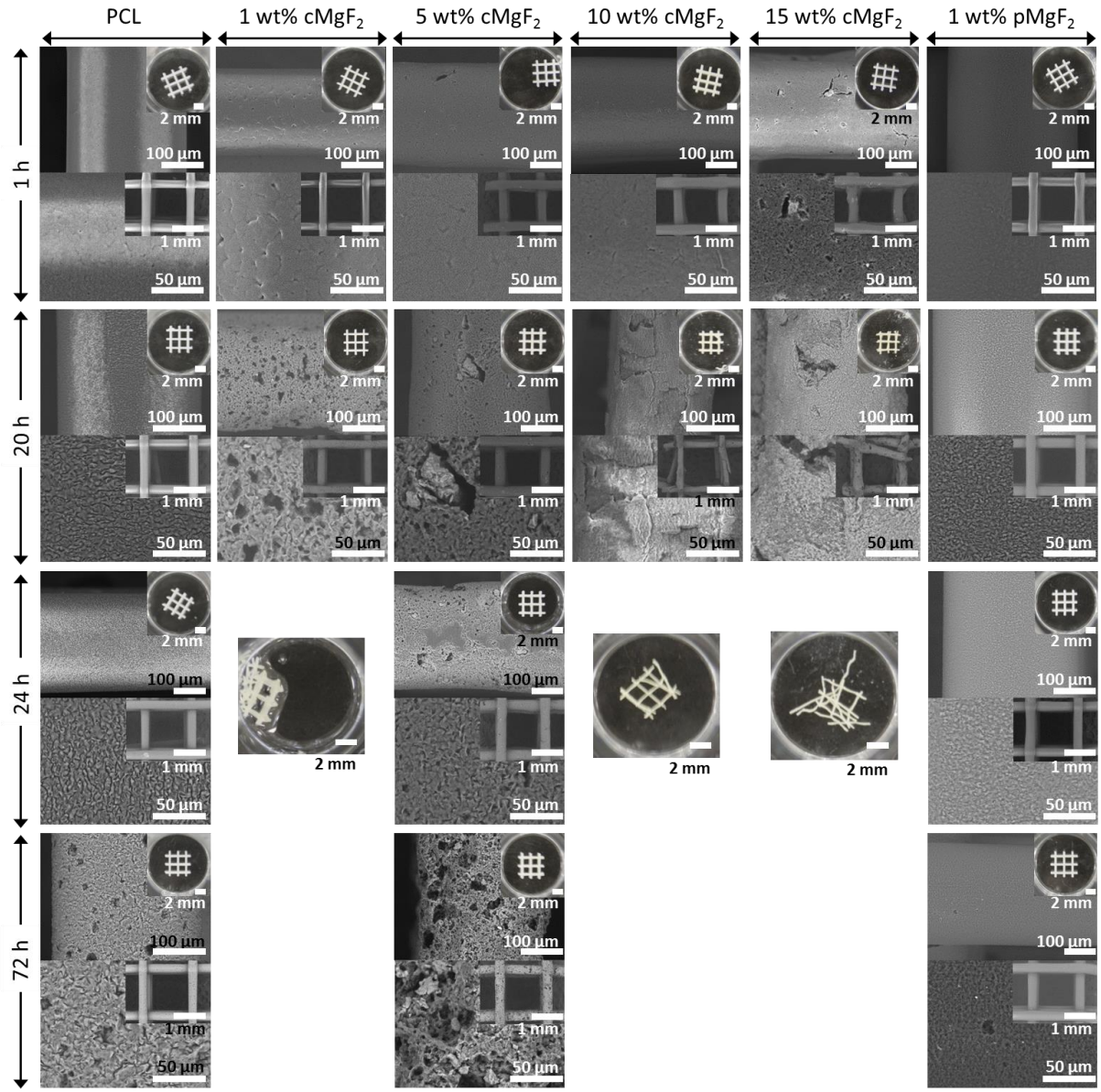

Figure S13. SEM images of FDM scaffolds after accelerated degradation at several time points: PCL/MBC is not shown because no morphology difference to pure PCL was obvious. Cf. to respective mass losses in Figure 4 (conditions: 5 M NaOH, 37 °C).

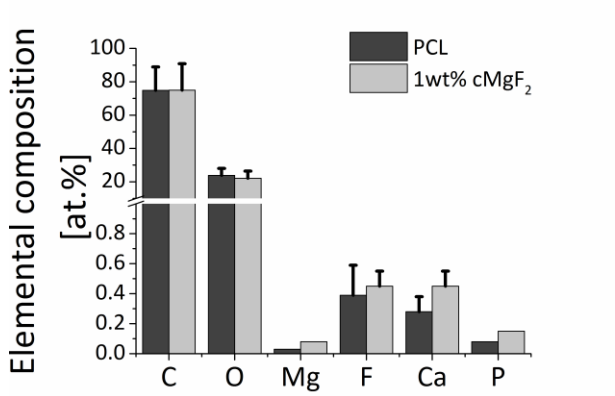

Figure S14. Elemental distribution by EDX after incubation in Mg-free MEM: Slight increase of Ca and P on the composite surface compared to pure PCL which might prove beneficial for osteoblastic bone forming processes.

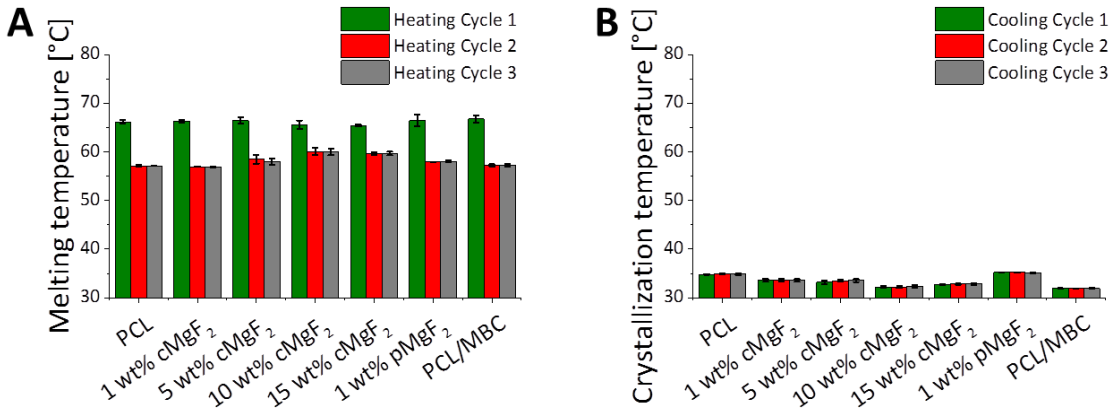

Figure S15. Dynamic scanning calorimetry results: (A) DSC melting temperature T_m and (B) crystallization temperatures T_c of three heating and cooling cycles. Additive manufacturing such as FDM had an influence on the melting temperatures in the first cycle, but no significant differences between the samples were observed.

References

[1] T. Schwemmer, J. Baumgartner, D. Faivre, H. G. Börner, *J. Am. Chem. Soc.* **2011**, *134*, 2385; F. Hanßke, E. Kemnitz, H. G. Börner, *Small* **2015**, *11*, 4303.

[2] M. Domingos, D. Dinucci, S. Cometa, M. Alderighi, P. J. Bártolo, F. Chiellini, *Int. J. Biomater.* **2009**, *2009*, 9.

[3] G. Hochleitner, J. F. Hümmer, R. Luxenhofer, J. Groll, *Polymer* **2014**, *55*, 5017.

[4] G. Hochleitner, A. Youssef, A. Hrynevich, N. Haigh Jodie, T. Jungst, J. Groll, D. Dalton Paul, in *BioNanoMaterials*, DOI: 10.1515/bnm-2015-0022 2016.

[5] O. Hartman, C. Zhang, E. L. Adams, M. C. Farach-Carson, N. J. Petrelli, B. D. Chase, J. F. Rabolt, *Biomaterials* **2010**, *31*, 5700.

[6] G. Kister, G. Cassanas, M. Bergounhon, D. Hoarau, M. Vert, *Polymer* **2000**, *41*, 925.

[7] P. Scherrer, *Göttinger Nachrichten Math. Phys.* **1918**, *2*, 98.

[8] V. Crescenzi, G. Manzini, G. Calzolari, C. Borri, *Eur. Polym. J.* **1972**, *8*, 449.

[9] K. K. Gupta, A. Kundan, P. K. Mishra, P. Srivastava, S. Mohanty, N. K. Singh, A. Mishra, P. Maiti, *Phys. Chem. Chem. Phys.* **2012**, *14*, 12844.

[10] W. C. Oliver, G. M. Pharr, *J. Mater. Res.* **2004**, *19*, 3.

[11] C. X. F. Lam, M. M. Savalani, S.-H. Teoh, D. W. Hutmacher, *Biomed. Mater.* **2008**, *3*, 034108.

[12] J. Patel, A. Shafiee, W. Wang, N.M. Fisk, K. Khosrotehrani, *Placenta*, **2014**, *35*, 969.